High accuracy radiative data for plasma opacities[1]

Sultana N. Nahar

Abstract: Opacity, which gives the measure of the radiation transport in plasmas, is caused by the repeated absorption and emission of the propagating radiation by the constituent plasma elements. Microscopically, opacity (κ) depends mainly on two radiative processes: (*i*) photo-excitation (bound-bound transition) and (*ii*) photo-ionization (bound-free transition) in addition to electron-photon scattering. The monochromatic opacity $\kappa(\nu)$ at photon frequency ν is determined by the atomic parameters, oscillator strengths (*f*), and photo-ionization cross sections ($\sigma_{\rm PI}$). However, total monochromatic opacity is obtained from summed contributions of all possible transitions from all ionization stages of all elements in the source. The calculation of accurate parameters for such a large number of transitions has been the main problem for obtaining accurate opacities. The overall mean opacity, such as the Rosseland mean opacity ($\kappa_{\rm R}$), depends also on the physical conditions, such as temperature, density, elemental abundances, and equation of state. The necessity for high-precision calculations for opacities may be exemplified by the existing problems, such as the determination of solar elemental abundances. With new computational developments under the Iron Project, we are able to calculate more accurate atomic parameters, such as oscillator strengths for large number of transitions using the relativistic Breit–Pauli *R*-matrix (BPRM) method. We are finding new features in photo-ionization, such as the existence of extensive and dominant resonant structures in the high-energy region not studied before. These new data should provide more accurate opacities in high-temperature plasmas and can be used to investigate the well-known solar abundance problem.

PACS Nos: 32.80.–t, 32.80.Fb, 33.70.Ca, 32.70.Cs

Résumé : L'opacité, qui donne la mesure du transport radiatif dans le plasma, est causée par l'absorption et l'émission répétée de la radiation par les constituants élémentaires du plasma. Au niveau microscopique, l'opacité (κ) dépend principalement de deux mécanismes radiatifs : (*i*) la photo-excitation (transition lié-lié) et (*ii*) la photoionisation (transition lié-libre) dans la diffusion électron-photon. L'opacité monochromatique $\kappa(\nu)$, à la fréquence ν du photon, est déterminée par les paramètres atomiques, les forces d'oscillateur (*f*) et les sections efficaces de photoionisation ($\sigma_{\rm PI}$). Cependant, l'opacité monochromatique totale est obtenue d'une somme des contributions de toutes les transitions possibles pour toutes les étapes d'ionisation de tous les éléments de la source. Le calcul précis de paramètres pour un si grand nombre de transitions est resté le problème central dans l'obtention de résultats précis d'opacité. L'opacité moyenne générale, telle l'opacité moyenne de Rosseland ($\kappa_{\rm R}$), dépend aussi des conditions physiques, comme la température, la densité, les abondances et l'équation d'état. On peut souligner le besoin pour des calculs plus précis d'opacité en mentionnant certains problèmes existants, comme la détermination des abondances solaires. Avec les nouveaux développement de capacité de calcul du projet Iron Project, nous somme capables d'évaluer plus précisément les paramètres optiques, comme les forces d'oscillateur pour un grand nombre de transitions, en utilisant la méthode de la matrice *R* relativiste de Breit–Pauli (BPRM). En photoionisation, nous trouvons de nouvelles caractéristiques, comme l'existence de structures résonantes extensives et dominantes dans la région de haute énergie, pas étudiée jusqu'à présent. Ces nouvelles données devraient fournir des opacités plus précises pour les plasmas de haute énergie et peuvent être utilisées pour investiguer le problème familier des abondances solaires.

[Traduit par la Rédaction]

1. Introduction

Opacity is an essential quantity in studying the astrophysical and laboratory plasmas with a radiation source. Propagating radiation slows down with opacity and becomes weaker as it travels out. It takes over a million years for the energetic gamma radiation created by the nuclear fusion in the core of a star to travel to the surface as visible light. Opacity provides information on internal structure, chemical composition, and evolution of states, such as the local thermodynamic equilibrium (LTE) of the plasmas. The calculation of total opacity requires considerable amount of atomic data, as it is the summed contributions of all possible radiative transitions, such as bound-bound and bound-free, from all ionization stages of all elements in the source.

Discrepancies existed between observed and theoretically calculated opacities obtained using atomic data calculated from simple approximations. The Los Alamos calculated opacities were incorrect by factors of 2 to 5, resulting in inaccurate stellar models. For example, Cepheid stars, which are important to determine distances in astronomy, could not be modeled. A plea was made for accurate opacity from accurate atomic parameters [1]. This initiated the Opacity Project (OP) [2, 3], an international collaboration of about 25

Received 31 August 2010. Accepted 14 January 2011. Published at www.nrcresearchpress.com/cjp on 6 May 2011.

S.N. Nahar. Department of Astronomy, The Ohio State University, Columbus, OH 43210, USA.

E-mail for correspondence: nahar@astronomy.ohio-state.edu.

[1]This article is part of a Special Issue on the 10th International Colloquium on Atomic Spectra and Oscillator Strengths for Astrophysical and Laboratory Plasmas.

scientists from 6 countries and the OPAL (e.g., [4]) in the early 1980s.

The OP team extended the *R*-matrix codes, used mainly for collisional processes, to radiative processes [5]. It carried out the first systematic study and computation for atomic data for energy levels, oscillator strengths, and photo-ionization cross sections for all astrophysically abundant atoms and ions from hydrogen to iron using ab initio close-coupling (CC) approximation. The work resulted in a large amount of atomic data that are available in the TOPbase database [6]. The data were used to calculate the monochromatic opacities and Rosseland mean opacities available at the OPServer [7] at the Ohio Supercomputer Center. The effort solved the problem of computing the pulsation ratios of Cepheid variables. The opacities from the OP and the OPAL showed agreement. However, the OP provided the most detailed results on the radiative processes for most of the atoms and ions for the first time. New features in photo-ionization cross sections were revealed.

The next international collaboration of the Iron Project (IP) [8] is focused on both the radiative and collisional processes, but mainly for the astrophysically abundant iron and iron-peak elements. In contrast to earlier nonrelativistic LS coupling approach under the OP, IP includes relativistic fine structure effects, and the *R*-matrix method was extended to the Breit–Pauli *R*-matrix (BPRM) method [9]. Extensive sets of radiative and collisional data are being obtained under the IP. Most of these data are available at the TIPbase database [10], databases of journals *Astronomy and Astrophysics*, *Atomic Data and Nuclear Data Tables*, and at the NORAD-atomic-data site [11]. Although data from the OP and IP continue to solve many problems, such as the spectral analysis of black hole environments, the abundances of elements in astronomical objects, opacities, dark matter, there are outstanding problems, such as solar abundances discussed below, that remain to be solved, and will need more accurate and complete atomic data.

2. The need for highly accurate atomic data

The sun is the most studied star, yet there are remarkable differences between its calculated and measured opacities. The boundary of the solar convection zone, R_{CZ}, beyond which photons escape, is known to be accurately measured from helioseismology as 0.713 (relative to the total solar radius). R_{CZ} can also be calculated from radiation transport or opacity through elemental abundances in the solar plasma. The calculated boundary R_{CZ} is 0.726, a much larger value than the measured value. It is found that a 1% change in opacity leads to observable changes in R_{CZ}. Recent determination of abundances of light elements, carbon, nitrogen, oxygen, etc., are up to 30%–50% lower than the standard values long supported by astrophysical models, helioseismology, and meteoritic measurements.

Laboratories, with high-power lasers beams at the National Ignition Facility (NIF) or a Z-pinch machine at the Sandia National Lab, are now able to study radiation transport or opacity in fusion plasma experiments, where the plasma temperature and density are comparable to those at the solar convection zone. Recently Bailey et al. [12] reported achieving HED (high energy density) plasmas at temperature $T > 10^6$ K and density $N > 10^{20}$ cm^{-3}, similar to those at the boundary of the solar convection zone. At this HED condition, iron ions, such as Fe XVII, Fe XVIII, and Fe XIX, are abundant. Their [12] measured transmission spectra show significant differences in iron opacities compared with the calculated opacities obtained using atomic data from the OP. The calculated κ is much lower than the observed values, indicating the inaccuracy in the absorption continuum, that is, in photo-ionization cross sections at higher energies.

These measurements will enable the calibration of the theoretical calculations of basic parameters that govern opacity. Nahar and Pradhan [13] calculated monochromatic opacities for Fe IV at a temperature $\log T(K) = 4.5$ and electron density $\log N_e$ cm^{-3} = 17.0, where Fe IV dominates the iron opacity. With use of more accurate and larger number of transitions, they found that κ_ν, which depends primarily on oscillator strengths, differs considerably from those obtained using earlier transition parameters from the OP, as shown in Fig. 1. κ_ν varies over orders of magnitude between 500–4000 Å. A comparison indicates a systematic shift in groups of OP energies.

Considerable progress in computational capability is being made under the Iron Project to achieve for higher accuracy. More relativistic correction terms have been added to the BPRM method. Theoretical spectroscopy has been developed to consider a large number of fine structure levels for all practical purposes. We will illustrate results from recent calculations showing more complete and accurate atomic data and new features not studied before. These should facilitate the computation of more accurate monochromatic opacities.

3. Theory

First we will discuss atomic processes that cause opacity in plasmas. We will then describe briefly the ab initio method of the CC approximation with *R*-matrix that is used under the IP to calculate the atomic parameters for the radiative processes relevant to opacity calculations.

3.1 Atomic processes that determine opacity

The monochromatic opacity $\kappa(\nu)$ depends primarily on two radiative processes, (*i*) photoexcitation for bound-bound transition and (*ii*) photo-ionization for bound-free transitions. The oscillator strengths f_{ij} for photoexcitation, given by,

$$X^{+Z} + h\nu \rightarrow X^{+Z*} \tag{1}$$

where X^{+Z} is an ion of charge Z and asterisks indicate excitation, are related to $\kappa(\nu)$ by the following,

$$\kappa_\nu(i \rightarrow j) = \frac{\pi e^2}{mc} N_i f_{ij} \phi_\nu \tag{2}$$

N_i is the ion density in state i, and ϕ_ν is a profile factor (Gaussian, Lorentzian, or a combination of both) over a small wavelength range.

Photoinization can occur directly as a bound-continuum transition,

$$X^{+Z} + h\nu \rightarrow X^{+Z+1} + e \tag{3}$$

It also occurs through an intermediate doubly excited quasi-bound auto-ionizing state,

Fig. 1. (bottom) Monochromatic opacities (κ_ν) of Fe IV using atomic transitions from the Opacity Project in TOPbase and (top) using data from later calculations under the Iron Project [13] showing considerable differences, especially in region of 500–4000 Å.

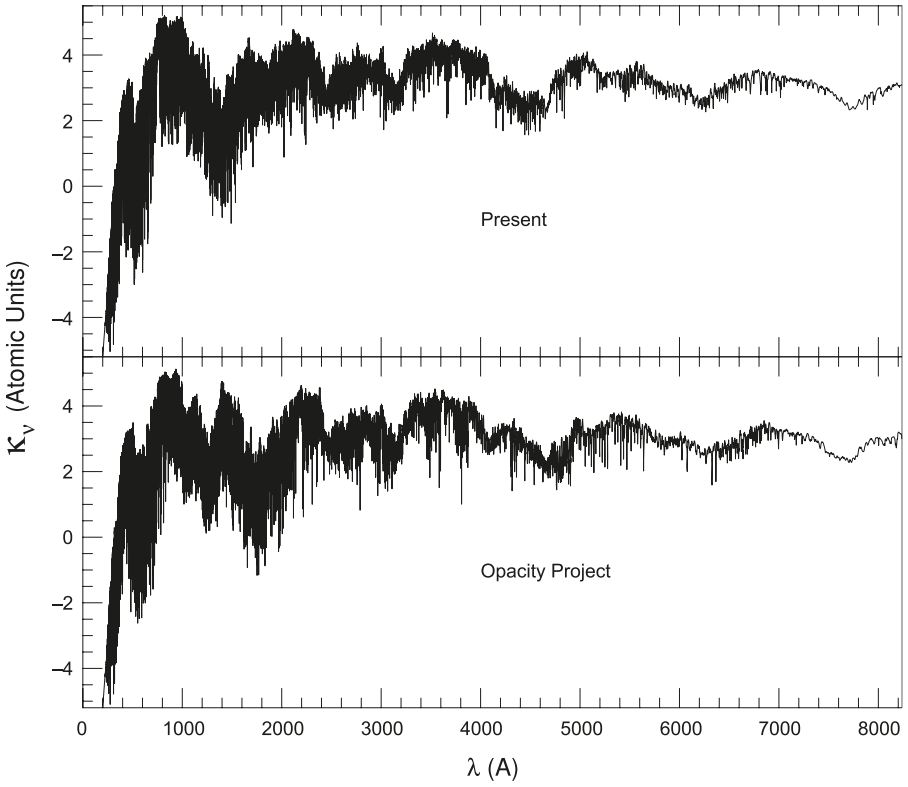

$$e + X^{+Z} \leftrightarrow (X^{+Z-1})^{**} \leftrightarrow \begin{cases} e + X^{+Z} & \text{AI} \\ X^{+Z-1} + h\nu & \text{DR} \end{cases} \tag{4}$$

where AI is autoionization and DR is dielectronic recombination, the inverse of which is photo-ionization. $\kappa(\nu)$ for photo-ionization is obtained from photo-ionization cross section $\sigma_{\rm PI}$ as,

$$\kappa_\nu = N_i \sigma_{\rm PI}(\nu) \tag{5}$$

κ_ν depends also on two other processes: (*i*) inverse Bremsstrahlung free-free (ff) scattering and (*ii*) photon-electron scattering. The radiation emitted by an accelerated electronic charged particle in an electromagnetic field is known as Bremsstrahlung. The inverse process is that a free electron and ion system can absorb a photon in an ff interaction, that is,

$$h\nu + [X_1^+ + e(\epsilon)] \rightarrow X_2^+ + e(\epsilon') \tag{6}$$

Explicit calculations for the ff scattering cross sections may be done using the elastic scattering matrix elements for the electron impact excitation of ions. More detailed discussion on this process and computation of the scattering matrix through the *R*-matrix method can be found in [2, 5]. An approximate expression for the ff opacity is given by,

$$\kappa_\nu^{\rm ff}(1,2) = 3.7 \times 10^8 N_e N_i g_{\rm ff} \frac{Z^2}{T^{1/2}\nu^3} \tag{7}$$

where $g_{\rm ff}$ is a Gaunt factor. The photon electron scattering is of two types. Thomson scattering, which is the most common event, happens when the electron is free and Rayleigh scattering happens when the electron is bound to an atomic or molecular species. κ is related to Thomson scattering cross section $\sigma^{\rm TH}$ as,

$$\kappa({\rm sc}) = N_e \sigma^{\rm Th} = N_e \frac{8\pi e^4}{3m^2c^4} = N_e\, 6.65 \times 10^{-25}\ {\rm cm^2/g} \tag{8}$$

and to Rayleigh scattering cross section $\sigma^{\rm R}$ as,

$$\kappa_\nu^{\rm R} = n_i \sigma_\nu^{\rm R} \approx n_i f_{\rm t} \sigma^{\rm Th} \left(\frac{\nu}{\nu_{\rm I}}\right)^4 \tag{9}$$

where n_i is the density of the atomic or molecular species, $h\nu_{\rm I}$ is the binding energy, and $f_{\rm t}$ is the total oscillator strength associated with the bound electron, i.e., the sum of all possible transitions, such as the Lyman series of transitions $1{\rm s} \rightarrow n{\rm p}$ in hydrogen.

The equation of state (EOS) gives the ionization fractions and level populations of each ion of an element in levels with non-negligible occupation probability. Some details of the opacity calculations can be found in [14].

The average opacity, such as the Rosseland mean $\kappa_{\rm R}(T, \rho)$, depends on the physical conditions of the plasma, temperature T and density ρ. $\kappa_{\rm R}(T, \rho)$ is the harmonic mean opacity averaged over the Planck function $g(u)$,

$$\frac{1}{\kappa_{\rm R}} = \frac{\int_0^\infty (1/\kappa_\nu) g(u) {\rm d}u}{\int_0^\infty g(u) {\rm d}u} \tag{10}$$

where $g(u)$ is given by

$$g(u) = \frac{15}{4\pi^4}\frac{u^4 e^{-u}}{(1-e^{-u})^2}, \qquad u = \frac{h\nu}{kT} \tag{11}$$

$g(u)$, for an astrophysical state, is calculated with different chemical compositions H (X), He (Y), and metals (Z), such that

$$X + Y + Z = 1 \tag{12}$$

3.2 Breit–Pauli *R*-matrix method

We calculate the oscillator strengths and photo-ionization cross sections using the Breit–Pauli R-matrix method in the CC approximation. The wave functions and energies of a multi-electron system are obtained by solving the equation,

$$H^{\mathrm{BP}}\Psi_E = E\Psi_E \tag{13}$$

where the relativistic Breit–Pauli Hamiltonian is given by,

$$H^{\mathrm{BP}} = H^{\mathrm{NR}} + H^{\mathrm{mass}} + H^{\mathrm{Dar}} + H^{\mathrm{so}} + \frac{1}{2}\sum_{i\neq j}^{N}\left[g_{ij}(so+so') + g_{ij}(ss') + g_{ij}(css') + g_{ij}(d) + g_{ij}(oo')\right] \tag{14}$$

and H^{NR} is the nonrelativistic Hamiltonian,

$$H^{\mathrm{NR}} = \sum_{i=1}^{N}\left\{-\nabla_i^2 - \frac{2Z}{r_i} + \sum_{j>i}^{N}\frac{2}{r_{ij}}\right\} \tag{15}$$

The Breit–Pauli R-matrix method [8, 9] includes the three one-body relativistic correction terms in the Hamiltonian,

$$H_{N+1}^{\mathrm{BP}} = H_{N+1}^{\mathrm{NR}} + H_{N+1}^{\mathrm{mass}} + H_{N+1}^{\mathrm{Dar}} + H_{N+1}^{\mathrm{so}} \tag{16}$$

where the mass correction, Darwin, and interaction terms are

$$H^{\mathrm{mass}} = -\frac{\alpha^2}{4}\sum_i p_i^4$$

$$H^{\mathrm{Dar}} = \frac{\alpha^2}{4}\sum_i \nabla^2\left(\frac{Z}{r_i}\right)$$

$$H^{\mathrm{so}} = \left[\frac{Ze^2\hbar^2}{2m^2c^2r^3}\right] \tag{17}$$

The spin-orbit interaction H^{so} splits LS energy into fine structure levels. The notation is s for spin and a prime indicates "other", o for orbit, c for contraction, and d for Darwin.

The inclusion of two-body interaction terms is much for complicated. However, these terms become important when the interaction is weak and when relativistic effects are important. In the latest BPRM codes[2] , the two-body Breit interaction term is,

$$H^{\mathrm{B}} = \sum_{i>j}\left[g_{ij}(so+so') + g_{ij}(ss')\right] \tag{18}$$

where

$$g_{ij}(so+so') = -\alpha^2\left[\left(\frac{\boldsymbol{r}_{ij}}{r_{ij}^3}\times\boldsymbol{p}_i\right)\cdot(\boldsymbol{s}_i + 2\boldsymbol{s}_j) + \left(\frac{\boldsymbol{r}_{ij}}{r_{ij}^3}\times\boldsymbol{p}_j\right)\cdot(\boldsymbol{s}_j + 2\boldsymbol{s}_i)\right]$$

$$g_{ij}(ss') = 2\alpha^2\left[\frac{\boldsymbol{s}_i\cdot\boldsymbol{s}_j}{r_{ij}^3} - 3\frac{(\boldsymbol{s}_i\cdot\boldsymbol{r}_{ij})(\boldsymbol{s}_j\cdot\boldsymbol{r}_{ij})}{r_{ij}^5}\right] \tag{19}$$

In the CC approximation, the ion is treated as a system of $(N + 1)$ electrons: a target or the ion core of N electrons with the additional interacting $(N+1)$th electron. The total wave function expansion is expressed as,

$$\Psi_E(\mathrm{e}+\mathrm{ion}) = A\sum_i^N \chi_i(\mathrm{ion})\theta_i + \sum_j c_j\Phi_j(\mathrm{e}+\mathrm{ion}) \tag{20}$$

where χ_i is the target ion or core wave function, calculated from atomic structure calculations, e.g., SUPERSTRUCTURE (SS) [15], θ_i is the interacting electron wave function (continuum or bound), and Φ_j is a correlation function of (e+ion). The complex resonant structures in the atomic processes are included through the coupling of bound and continuum channels. The substitution of Ψ_E(e+ion) in $H\Psi_E = E\Psi_E$ results in a set of coupled equations that are solved by the R-matrix method.

In the R-matrix method (Fig. 2), space is divided in two regions, the inner and the outer regions of a sphere of radius r_{a} with the ion at the center. The radius r_{a} is chosen large enough for the electron-electron interaction potential to be zero outside the boundary. The wave function at $r > r_{\mathrm{a}}$ is Coulombic, due to perturbation from the long-range multipole potentials. In the inner region, the partial wave function of the interacting electron is expanded in terms of a basis set, called the R-matrix basis, $F_i = \sum a_k u_k$, which satisfy,

$$\left[\frac{\mathrm{d}^2}{\mathrm{d}r^2} - \frac{l(l+1)}{r^2} + V(r) + \epsilon_{lk}\right]u_{lk} + \sum_n \lambda_{nlk}P_{nl}(r) = 0 \tag{21}$$

and are made continuous at the boundary by matching with the Coulomb functions outside the boundary. For negative energy, the solution is a bound (e+ion) state Ψ_{B}, and for positive energy, the solution is a continuum state Ψ_{F}.

3.3 Atomic quantities

The dipole transition matrix elements for photo-excitation and photo-ionization are,

$$\langle\Psi_{\mathrm{B}}||\mathbf{D}||\Psi_{B'}\rangle, \qquad \langle\Psi_{\mathrm{B}}||\mathbf{D}||\Psi_{\mathrm{F}}\rangle \tag{22}$$

respectively, where $D = \sum_i r_i$ is the dipole operator, and the sum is over the number of electrons. The reduced tensor $||\mathbf{D}||$ gives 3 j symbols for angular momenta on simplification. The transition matrix element reduces to generalized line strength as,

$$S = \left|\left\langle\Psi_f\left|\sum_{j=1}^{N+1} r_j\right|\Psi_i\right\rangle\right|^2 \tag{23}$$

[2]Following astrophysical nomenclature, we abbreviate the singular form planetary nebula as "PN" and the plural form as "PNe".

Fig. 2. Space consideration in the *R*-matrix method.

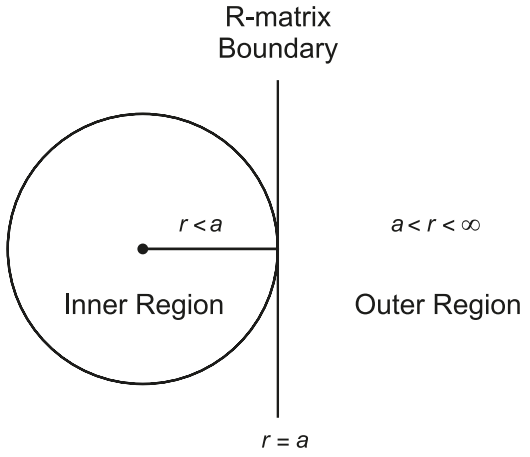

This is the quantity of interest for both processes.

The oscillator strength (f_{ij}) and radiative decay rate (A_{ji}) for the bound-bound transition are obtained as,

$$f_{ij} = \left[\frac{E_{ji}}{3g_i}\right] S$$

$$A_{ji}(\text{sec}^{-1}) = \left[0.8032 \times 10^{10} \frac{E_{ji}^3}{3g_j}\right] S \tag{24}$$

The photo-ionization cross section, $\sigma_{\rm PI}$ is obtained as,

$$\sigma_{\rm PI} = \left[\frac{4\pi}{3cg_i}\right] \omega S \tag{25}$$

where ω is the incident photon energy in Rydberg units.

When relativistic fine structure effects are considered, BPRM method enables extensive sets of E1 transitions ($\Delta j = 0, \pm 1$, $\Delta L = 0, \pm 1, \pm 2$, parity π changes) with same-spin multiplicity ($\Delta S = 0$) and intercombination ($\Delta S \neq 0$). On the contrary, LS coupling allows only same-spin multiplicity transitions. The transitions with same-spin multiplicity are usually stronger than the intercombination transitions. However, with increased importance of relativistic effects, they are often of similar strength. Overall, the strengths of electric dipole transitions are orders of magnitude higher than those of higher order multipole transitions, known as the forbidden transitions. Hence, the electric dipole transitions contribute most and are the only transitions included in the opacity calculations.

Under the Iron Project, large sets of various forbidden transitions, which are due to higher order multipole terms in photon-ion interactions, are also considered in the Breit–Pauli approximation. Because of small *f*-values, the radiative decay rates are typically calculated for the forbidden transitions. These transitions are mainly:

1. electric quadrupole (E2) transitions ($\Delta J = 0, \pm 1, \pm 2$, parity does not change),

$$A_{ji}^{\rm E2} = 2.6733 \times 10^3 \frac{E_{ij}^5}{g_j} S^{\rm E2}(i,j)\text{s}^{-1} \tag{26}$$

2. magnetic dipole (M1) transitions ($\Delta J = 0, \pm 1$, parity does not change),

$$A_{ji}^{\rm M1} = 3.5644 \times 10^4 \frac{E_{ij}^3}{g_j} S^{\rm M1}(i,j)\text{s}^{-1} \tag{27}$$

3. electric octupole (E3) transitions ($\Delta J = 0, \pm 2, \pm 3$, parity changes),

$$A_{ji}^{\rm E3} = 1.2050 \times 10^{-3} \frac{E_{ij}^7}{g_j} S^{\rm E3}(i,j)\text{s}^{-1} \tag{28}$$

4. magnetic quadrupole (M2) transitions ($\Delta J = 0, \pm 2$, parity changes),

$$A_{ji}^{\rm M2} = 2.3727 \times 10^{-2} \frac{E_{ij}^5}{g_j} S^{\rm M2}(i,j)\text{s}^{-1} \tag{29}$$

More details of the forbidden transitions can be found in [14, 16]. These transitions are treated through atomic structure code SUPERSTRUCTURE [15] and its later version [17].

The lifetime of a level can be obtained easily from the values of A as,

$$\tau_k(s) = \frac{1}{\sum_i A_{ki}(\text{s}^{-1})} \tag{30}$$

4. Results and discussions

The accuracy and completeness of sets of oscillator strengths for bound-bound transitions and new features in photo-ionization affecting the plasma opacities are discussed in the subsections below.

4.1 Oscillator strengths from the iron project

Spectra of astronomical objects are rich in iron lines. Iron ions cause prominent features in their opacities. Due to the large number of closely lying energy levels, lines of various ionic states often overlap, making identification difficult. Under the IP, using the relativistic BPRM method, the radiative transitions of these ions are being computed and studied in detail for proper identification, astrophysical modeling, and opacity calculations. A few examples of the ions studied are Fe XVII [17], Fe XVIII [18], Fe XIX [19]. Through the computational power of the *R*-matrix method, which is capable of considering many states in the computation, oscillator strengths and radiative decay rates for extensive sets of transitions, typically with $n \leq 10$ and $l \leq 9$, are being obtained. These are more complete sets of transitions than the available published sets and are of comparable accuracy with the most accurate existing values.

The important issue of spectroscopic identification of the transitions should be addressed. While atomic structure calculations can identify any energy level based on the percentage contributions of the configurations, BPRM is not capable of such identification. A scheme developed by Nahar and Pradhan [20, 21], based on the channel contributions in the outer region of the *R*-matrix method, quantum defect theory and algebraic algorithms of fine structure components of a term can designate spectroscopic identifications of the fine structure energy levels. These match with those from atomic structure calculations for most cases. However, since BPRM considers larger number of configurations, causing more mix-

Table 1. Comparison of Fe XIX energies from the BPRM method with those from NIST.

Level		J: I_J	E_o (Ry, NIST)	E_c (Ry, BPRM)
$2s^22p^4$	$^3P^e$	2.0: 1	107.900 00	107.243 00
$2s^22p^4$	$^3P^e$	1.0: 1	107.085 00	106.430 00
$2s^22p^4$	$^3P^e$	0.0: 1	107.214 00	106.563 00
$2s^22p^4$	$^1D^e$	2.0: 2	106.361 00	105.669 00
$2s^22p^4$	$^1S^e$	0.0: 2	104.937 00	104.217 00
$2s2p^5$	$^3P^o$	2.0: 1	99.490 00	98.775 70
$2s2p^5$	$^3P^o$	1.0: 1	98.926 40	98.202 50
$2s2p^5$	$^3P^o$	0.0: 1	98.513 80	97.788 00
$2s2p^5$	$^1P^o$	1.0: 2	96.348 80	95.591 00
$2p^6$	$^1S^e$	0.0: 3	88.451 90	87.653 00
$2s^22p^3\ ^4S^o3s$	$^3S^o$	1.0: 3	47.027 40	46.321 00
$2s^22p^3\ ^2D^o3s$	$^3D^o$	3.0: 1	45.769 80	45.009 50
$2s^22p^3\ ^2D^o3s$	$^3D^o$	2.0: 3	46.052 30	45.340 50

Note: Data from [20].

Table 2. Comparison of f, S, A values of Fe XIX for allowed E1 transitions.

λ (Å)	A(s^{-1})(NIST and others)	A(s^{-1}) (Present) (BPRM, SS)	$C_i - C_j$	SLπ: $i - j$	g: $i - j$
108.355	3.9e+10[a]: C,3.57e+10[b]	3.35e+10, 3.54+10	$2s^22p^4 - 2s^2p^5$	$^3P - ^3P^o$	5–5
109.952	1.6e+10[c]: C	1.40e+10, 1.46+10	$2s^22p^4 - 2s^2p^5$	$^3P - ^3P^o$	1–3
111.695	1.26e+10[c]: C	1.09e+10, 1.15+10	$2s^22p^4 - 2s2p^5$	$^3P - ^3P^o$	3–3
119.983	1.04e+10[c]: C	9.02e+9, 8.54+9	$2s^22p^4 - 2s2p^5$	$^3P - ^3P^o$	3–5
101.55	3.17+10[c]: E,2.91e+10[b]	2.77e+10	$2s^22p^4 - 2s2p^5$	$^3P - ^3P$	5–3
78.888	1.3e+10[c]: E	1.12+10, 1.14+10	$2s^22p^4 - 2s2p^5$	$^3P - ^1P$	5–3
83.87	1.6e+09[c]: E	1.19E+09, 1.26+9	$2s^22p^4 - 2s2p^5$	$^3P - ^1P$	1–3
84.874	9.3e+08[c]: E	8.75e+08, 8.32+8,	$2s^22p^4 - 2s^2p^5$	$^3P - ^1P^o$	3–3
132.63	2.2e+09[a]: E	1.96e+9, 2.01+9	$2s^22p^4 - 2s2p^5$	$^1D - ^3P^o$	5–5
91.012	1.49e+11[c]: C	1.32e+11, 1.38e+11	$2s^22p^4 - 2s^2p^5$	$^1D - ^1P^o$	5–3
151.607	7.9e+08[c]: E	5.86e+8, 6, 65+8s	$2s^22p^4 - 2s2p^5$	$^1S - ^3P^o$	1–3
14.966	2.5e+12[a]: C	2.24e+12, 2.09e+12	$2s^22p^4 - 2s^22p^3(^4S)3s$	$^3P - ^3S$	5–3
14.929	2.5e+11[d]: D	2.45e+11, 2.77e+11	$2s^22p^4 - 2s^22p^3(^2D)3s$	$^3P - ^3D$	3–5
14.668	1.1e+12[d]: C	1.06e+12, 1.12+12	$2s^22p^4 - 2s^22p^3(^2P^o)3s$	$^3P - ^3P^o$	3–1
14.735	9.8e+11[d]: D,9.53e+11[b]	9.29e+11, 8.52+11	$2s^22p^4 - 2s^22p^3(^2D)3s$	$^3P - ^3D$	5–5
14.929	1.2e+12[d]: D	1.16e+12, 1.04e+12	$2s^22p^4 - 2s^22p^3(^2D)3s$	$^3P - ^3D$	3–3
14.633	1.4e+11[d]: E,1.27e+11[b]	1.18E+11	$2s^22p^4 - 2s^22p^3(^2D)3s$	$^3P - ^1D$	5–5
14.995	2.2e+12[d]: D	2.05e+12, 2.0e+12	$2s^22p^4 - 2s^22p^3(^2D)3s$	$^1D - ^1D$	5–5
14.534	6.8e+11[d]: D	6.36e+11, 6.05+11	$2s^22p^4 - 2s^22p^3(^2P)3s$	$^3P - ^3P$	3–5
14.603	7.5e+11[d]: D	6.94e+11, 6,53+11	$2s^22p^4 - 2s^22p^3(^2P)3s$	3P – 3P	1–3
14.668	1.1e+12[d]: C	1.07e+12, 9.74+11	$2s^22p^4 - 2s^22p^3(^2D^o)3s$	$^3P - ^3D^o$	5–7
14.70	6.8e+11[a]: E,6.49e+11[b]	5.05e+11, 5.22+11	$2s^22p^4 - 2s^22p^3(^2P^o)3s$	$^1D - ^3P^o$	5–5
14.806	5.6e+11[d]: E	5.05e+11, 4.88+11	$2s^22p^4 - 2s^22p^3(2P)3s$	$^1D - ^3P$	5–3
Lifetime (10^{-12}s)					
λ	Expt	Present	Others	Conf	Level
108.4	23.5±2[e]	22.48	22.5[f], 22.1[g], 17.6[h]	$2s2p^5$	$^3P^o_2$

Note: Data from [20].
[a]Shirai et al. (2000) [24]
[b]Jonauskas et al. (2004) [28]
[c]Cheng et al. (1979) [26]
[d]Fawcett (1986) [25]
[e]Buchet et al. (1980) [29]
[f]Safronova et al. (1975) [30]
[g]Feldman et al. (1975) [31]
[h]Smith et al. (1971) [32]

ing, coefficients and quantum defects are often too close to differentiate for closely lying levels, and identifications may differ. The difference can come from atomic structure calculations as well where identification also depends on the set of the configurations selected and the way configurations are optimized.

Table 3. Comparison of forbidden transitions (E2, M1, M2) of Fe XIX from the IP with other calculations.

λ (Å)	A(s^{-1}) (Others)	A(s^{-1}) (present)	$C_i - C_j$	SLπ *i-j*	*g i-j*
424.26	1.50e+05[a]: C,1.39e+05[b]	1.41e+5	$2s^22p^4 - 2s^22p^4$: *M*1	$^3P - ^1S$	3–1
592.234	6.00[a]: E,6.18[b]	6.0	$2s^22p^4 - 2s^22p^4$: *E*2	$^3P - ^1D$	5–5
592.234	1.73e+04 [a] : C,1.69e+04[b]	1.67e+4	$2s^22p^4 - 2s^22p^4$: *M*1	$^3P - ^1D$	5–5
639.84	4.9e+01[a]: E,4.83e+01[b]	4.92e+1	$2s^22p^4 - 2s^22p^4$: *E*2	$^1D - ^1S$	5–1
1118.06	0.611[a]: E,0.614[b]	0.635	$2s^22p^4 - 2s^22p^4$: *E*2	$^3P - ^3P$	5–3
1118.06	1.45e+04[a]: C,1.42e+04[c]	1.46e+4	$2s^22p^4 - 2s^22p^4$: *M*1	$^3P - ^3P$	5–3
1259.27	6.70e+02[a]: D,6.99e+02[b]	6.51e+2	$2s^22p^4 - 2s^22p^4$: *M*1	$^3P - ^1D$	3–5
1328.90	0.491[a]: E,0.509[b]	0.502	$2s^22p^4 - 2s^22p^4$: *E*2	$^3P - ^3P$	5–1
2207.8	4.820e+03[c]: C	4.96e+03	$2s2p^5 - 2s2p^5$: *M*1	$^3P^o - ^3P^o$	3–1
7045	4.0e+01[a]: C	41.0	$2s^22p^4 - 2s^22p^4$: *M*1	$^3P - ^3P$	1–3
353.532	9.4e+03[b]: D	8.79e+03	$2s2p^5 - 2s2p^5$: *M*1	$^3P^o - ^1P^o$	3–3
420.911	7.7e+03[c]: D,8.06e+03[b]	7.31e+03	$2s2p^5 - 2s2p^5$: *M*1	$^3P^o - ^1P^o$	1–3

Note: Data from [20].
[a]Cheng et al. (1979) [26]
[b]Jonauskas et al. (2004) [28]
[c]Loulergue et al. (1985) [27]

Table 4. Levels of Fe XVIII considered in photo-ionization calculations of Fe XVII.

i	Configuration	Term	2*J*	*E* (Ry) Present	*i*	Configuration	Term	2*J*	*E* (Ry) Present
n = 2 states					30	$2s^22p^43p$	$^2P^o$	1	61.899
1	$2s^22p^5$	$^2P^o$	3	0.00000	31	$2s^22p^43d$	^4D	5	62.299
2	$2s^22p^5$	$^2P^o$	1	0.93477	32	$2s^22p^43d$	^4D	7	62.311
3	$2s2p^6$	^2S	1	9.70228	33	$2s^22p^43d$	^4D	1	62.906
n = 3 states					34	$2s^22p^43d$	^4D	3	63.050
4	$2s^22p^43s$	^4P	5	56.690	35	$2s^22p^43p$	$^2P^o$	3	62.461
5	$2s^22p^43s$	^2P	3	56.936	36	$2s^22p^43d$	^4F	9	62.535
6	$2s^22p^43s$	^4P	1	57.502	37	$2s^22p^43d$	^2F	7	62.629
7	$2s^22p^43s$	^4P	3	57.572	38	$2s^22p^43p$	$^2P^o$	1	62.686
8	$2s^22p^43s$	^2P	1	57.798	39	$2s^22p^43d$	^4P	1	62.496
9	$2s^22p^43s$	^2D	5	58.000	40	$2s^22p^43d$	^4P	3	62.625
10	$2s^22p^43s$	^2D	3	58.355	41	$2s^22p^43d$	^4F	5	62.985
11	$2s^22p^43p$	$^4P^o$	3	59.209	42	$2s^22p^43d$	^2P	1	63.123
12	$2s^22p^43p$	$^4P^o$	5	59.238	43	$2s^22p^43d$	^4F	3	63.156
13	$2s^22p^43p$	$^4P^o$	1	59.478	44	$2s^22p^43d$	^2F	5	62.698
14	$2s^22p^43p$	$^4D^o$	7	59.525	45	$2s^22p^43d$	^4F	7	63.271
15	$2s^22p^43p$	$^2D^o$	5	59.542	46	$2s^22p^43d$	^2D	3	63.302
16	$2s^22p^43s$	^2S	1	59.916	47	$2s^22p^43d$	^4P	5	62.911
17	$2s^22p^43p$	$^2F^o$	1	59.982	48	$2s^22p^43d$	^2P	3	63.308
18	$2s^22p^43p$	$^4D^o$	3	60.005	49	$2s^22p^43d$	^2D	5	63.390
19	$2s^22p^43p$	$^4D^o$	1	60.012	50	$2s^22p^43d$	^2G	7	63.945
20	$2s^22p^43p$	$^2D^o$	3	60.147	51	$2s^22p^43d$	^2G	9	63.981
21	$2s^22p^43p$	$^4D^o$	5	60.281	52	$2s^22p^43d$	^2S	1	63.919
22	$2s^22p^43p$	$^2P^o$	3	60.320	53	$2s^22p^43d$	^2F	5	64.200
23	$2s^22p^43p$	$^2S^o$	1	60.465	54	$2s^22p^43d$	^2F	7	64.301
24	$2s^22p^43p$	$^4S^o$	3	60.510	55	$2s^22p^43d$	^2P	3	64.138
25	$2s^22p^43p$	$^2F^o$	5	60.851	56	$2s^22p^43d$	^2D	5	64.160
26	$2s^22p^43p$	$^2F^o$	7	61.028	57	$2s^22p^43d$	^2D	3	64.391
27	$2s^22p^43p$	$^2D^o$	3	61.165	58	$2s^22p^43d$	^2P	1	64.464
28	$2s^22p^43p$	$^2D^o$	5	61.272	59	$2s^22p^43d$	^2D	5	65.305
29	$2s^22p^43p$	$^2P^o$	3	61.761	60	$2s^22p^43d$	^2D	3	65.468

In the latest IP work on Fe XIX [19], the BPRM method produced 1626 fine structure levels with $n \leq 10$ and $l \leq 9$, compared with the available 63 observed levels (NIST table [22]). All these fine structure levels have been identified spectroscopically. The BPRM energies are of comparable accuracy, with the most accurate available values agreeing with the observed values within 4%, as shown in Table 1.

The bound levels of Fe XIX correspond to 289 291 allowed electric dipole transitions over a broad energy range. Table 2 presents a sample set of comparisons between

BPRM transition parameters and other available values. E1 transitions from SS, from the same work [19], are also given for comparison. Although available values are marked with various accuracy ratings by the NIST, BPRM values show good agreement with these and to the recent calculations, for most cases. A single measurement of lifetime of level $2s2p^5(\,^3P^o_2)$ is also in good agreement with the BPRM value. More detailed comparisons can be found in Nahar [19].

The IP work by Nahar [19] also considered the forbidden transitions. With a set of 379 fine structure levels from its ground and 15 excited configurations, a total of 66 619 transitions of type E2, E3, M1, and M2 were reported. Table 3 shows a comparison of the IP forbidden transitions with the existing values with very good agreement.

4.2 Photo-ionization

Opacity due to photo-ionization is caused mainly by photon absorption through resonances. These resonances arise from excitations of the core with increased photon energy. The OP work considered the resonances in the photo-ionzation of the ground and many excited states of an atomic system for the first time. However, the work included only the low-energy resonances. It was assumed that most of the dominant couplings of channels lie with the lower excitations of the core ion, particularly with states in the same complex, $\Delta n = 0$. The computational limit, although not extreme, was also an issue. However, later investigations under the IP revealed that high-lying core excitations could play a very important role, as cases have been found where these excitations introduce extensive and high-peak resonances.

Relativistic fine structure effects at low energy are also found to reveal structures not allowed in the LS coupling approximation. These structures, not studied before, can be very important for low-temperature plasmas, where they will change the current calculated opacities and expect to resolve or reduce large gaps in differences between the observed and calculated values. We illustrate these new features in the following two sections.

4.2.1 High-energy photo-ionization

The example case for high-energy photo-ionization are the latest BPRM calculations of photo-ionization cross sections (σ_{PI}) of Fe XVII [32]. The ion is abundant in solar corona. The core ion, Fe XVIII, has three levels in the $n = 2$ complex, beyond which there is a large energy gap of about 47 Ry, before the core can be excited to $n = 3$ levels, as seen in Table 4. The table presents 60 levels of Fe XVIII, considered in calculations of photo-ionization cross sections. The very high-lying $n = 3$ levels were assumed to have small coupling effects on photoinization in earlier calculations.

The BPRM calculations for Fe XVII found 454 bound fine structure levels of the ion, where $n \le 10$, $l \le 9$, $J \le 8$. This number for bound levels remains the same whether only 3 levels of $n = 2$ or 60 levels of $n = 2$, 3 complexes of the core are considered in the computation. The reason is that all bound levels are formed with core $n = 2$ core levels. The $n = 3$ core levels lie too high above to form any bound level. These are reasons for not considering $n = 3$ levels in the previous OP calculation.

Although $n = 3$ core excitations do not form any bound state, they form auto-ionizing states and appear as resonances

Fig. 3. Photo-ionization cross sections of the Fe XVII, (*a*) ground level $2s^22p^6(^1S_0)$, (*b*) excited level $2s^22p^53d(\,^3P^o_0)$, illustrating the effects of core excitations in $n = 2$ and $n = 3$ core levels [32].

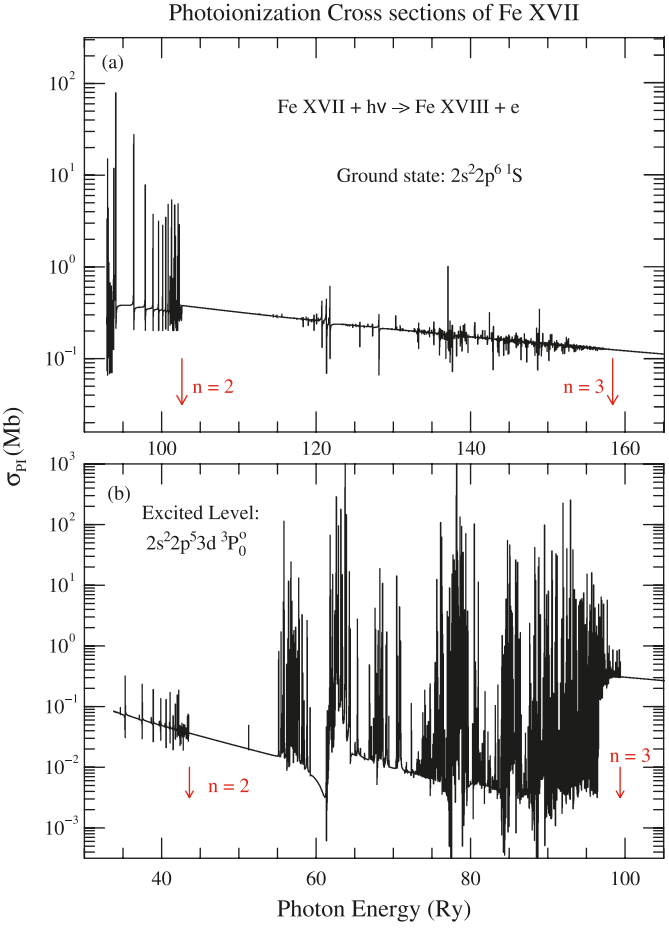

in photo-ionization cross section. The auto-ionizing states of $n = 3$ levels do not have much impact, except appearing as some weak resonances on the ground level σ_{PI} of Fe XVII, shown in the top panel of Fig. 3. The figure presents σ_{PI} of the (*a*) ground level $2s^22p^6(^1S_0)$ and (*b*) an excited level $2s^22p^53d(\,^3P^o_0)$ of Fe XVII. In the figure, arrows indicate the energy limits of $n = 2$ and 3 core states. While resonances introduced by the core excitations to $n = 2$ levels are important for the ground level, excitations to $n = 3$ levels are more important for the excited level photo-ionization. The high-energy region of σ_{PI} of the excited level is filled with high peak resonances.

In Fig. 4 the photo-ionization cross section of level $2s^22p^53d(\,^3P^o_0)$ is compared with that of state $2s^22p^53d(^3P^o)$ obtained under the OP and available at the TOPbase [6]. Although OP data corresponds to the LS state $^3P^o$, they can be compared with σ_{PI} of the component level $^3P^o_0$, since other components show similar features. Comparison shows extensive resonances with enhanced background in the high-energy region, which are missing in the OP cross sections. These high-peak resonances in BPRM cross sections indicate high absorption of photons by orders of magnitude, that is, increased opacity that would be grossly underestimated through use of the OP data.

Fig. 4. Comparison of photo-ionization cross section σ_{PI} of Fe XVII: (*a*) OP data of state $2s^22p^53d(^3P^o)$, (*b*) BRPM data of level $2s^22p^53d(\,^3P^o_0)$ from the recent *R*-matrix calculations.

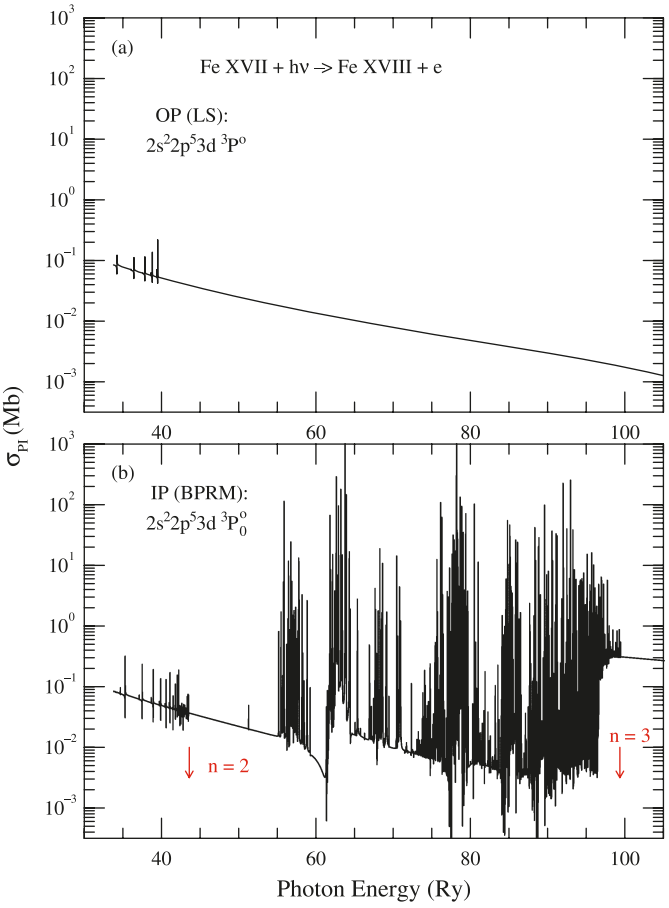

Fig. 5. Total photo-ionization cross section σ_{PI} of excited levels of Fe XVII, $2s^22p^5nf(^3D_1)$ with nf = 5f, 7f, 9f. σ_{PI} decreases monotonically with increased energies, but rises considerably as the energy approaches the core excitation for a PEC or Seaton resonance. Seaton resonances enhance the background cross section considerably, by orders of magnitude. The figure shows 29 overlapped PEC positions, where two arrows highlight the peaks.

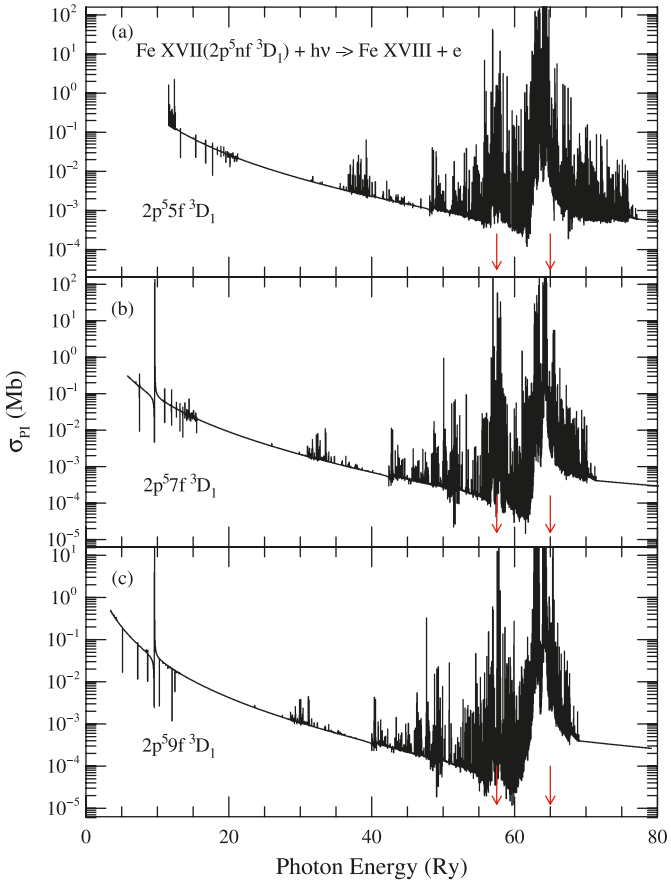

The wide PEC (photo-excitation of core) or Seaton resonances in the high-energy region are the other dominant contributors to plasma opacity. These resonances occur when the core goes through a dipole-allowed transition, while the outer electron remains a spectator. The state is followed by ionization via the outer electron, while the core drops down to the ground state. PEC resonances are manifested at the excited energy threshold that the core was excited to. The resonant phenomena was first explained by Seaton in [33]. Figure 5 presents σ_{PI} of three excited levels of Fe XVIII, $2s^22p^5nf(^3D_1)$ with nf = 5f, 7f, and 9f. From Table/4, it can be seen that there are 29 possible dipole-allowed transitions for the core ground level, and each corresponds to a Seaton resonance. The overlapping Seaton resonances are indicated by a couple of arrows in the figure. As the figure shows, Seaton resonances are strong, which increases the background cross sections by orders of magnitude. The shape and strength of PEC resonances depend on the interference of core excitations and overlapping Rydberg series of resonances. These dominating features, causing greatly enhanced photon absorptions relevant to the opacities, are non-existent in the available data, thereby grossly underestimating the opacity.

4.2.2 Low-energy photo-ionization

Relativistic effects are not significant for low- to medium-*Z* elements for most practical applications. Hence photo-ionization cross sections calculated in LS coupling can be of high accuracy, to benchmark experimental measurement with very good agreement. However, there are cases when resonant features are formed by the fine structure coupling only, that is, they are not allowed in LS coupling in the very low-energy region and are of crucial importance.

An example of such a case is the photo-ionization of O II. The importance of O II as a diagnostic element is well-known for low-temperature plasmas in the Orion nebula from where its lines can be observed. O II has been thoroughly studied for its radiative and collisional processes. The experimental measurement of O II photo-ionization at the high-resolution set-up of ALS (Advanced Light Source) in Berkeley has been benchmarked with theoretical values in LS coupling. However, determination of its abundance is an unsolved problem, since there is a large discrepancy between the abundances calculated from collisional excitation and from recombination processes.

Fig. 6. Near-threshold resonances in photo-ionization cross sections (σ_{PI}) of the ground level $2p^3\ {}^4S^o_{3/2}$ of O II in the energy region of the O III ground-state fine structure levels: (*a*) featureless total σ_{PI} (LS), (*b*) total σ_{PI} (BPRM), (*c*)-(*e*) partial σ_{PI} for photo-ionization into fine structure components $2p^2\ {}^3P_{0,1,2}$ of O III, with arrows indicating the ionization thresholds [34].

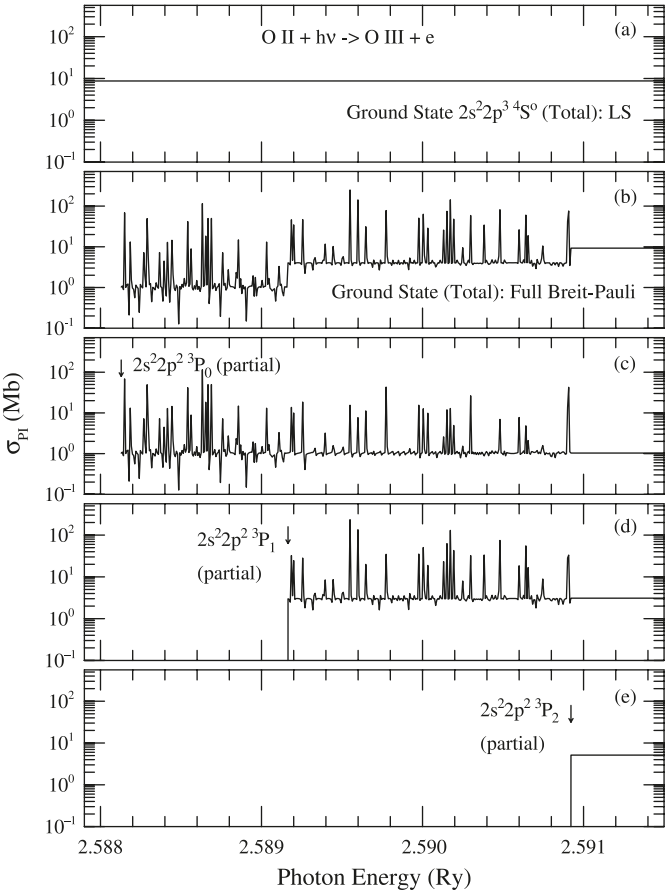

Fig. 7. Photo-ionization cross sections, σ_{PI} of the excited $2s2p^3(^5S^o)$ state of Fe XXI [4]. The narrow, high peak resonances below the first excited core threshold $2s2p^2(^4P)$ (indicated by arrow) are due to fine structure couplings but non-existent in the LS-coupling approximation.

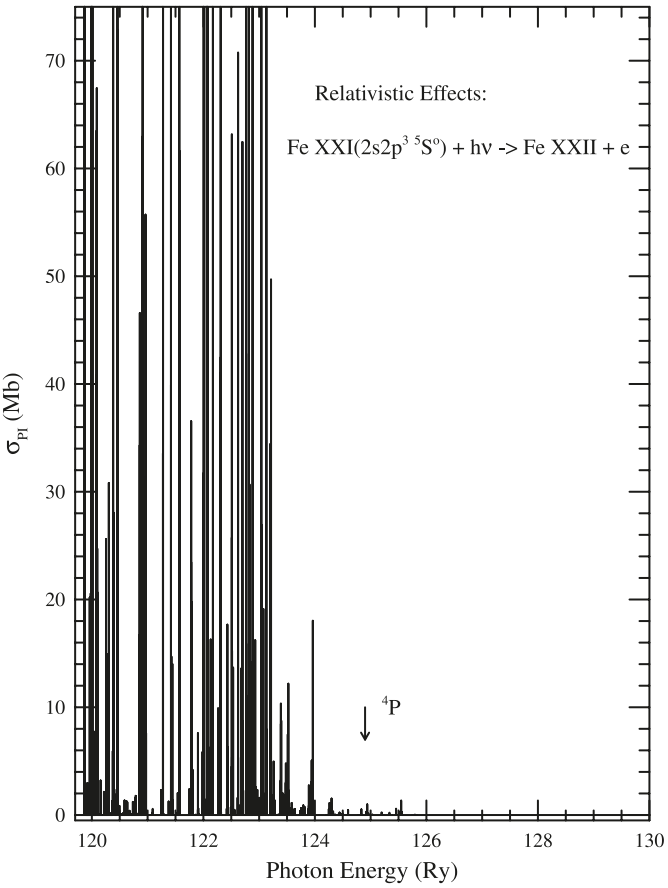

The latest calculations, including relativistic fine structure, for O II photo-ionization in the very low-energy region near the ionization threshold has revealed crucial resonant structures formed by the fine structure couplings. Figure 6 shows σ_{PI} of the $2s^22p^3(\ {}^4S^o_{3/2})$ ground state of O II in the low-energy region. The top panel shows σ_{PI} in LS coupling, which is a smooth line without any features [35]. But panel (*b*) presents total σ_{PI} from the relativistic BPRM method, where contributions of the full Breit–Pauli interaction have been included [34]. Figure 6*b* shows the resonant features as well as the background jump at each core ionization threshold $^3P_0$, $^3P_1$, and $^3P_2$ of O III. These resonant structures make very important contributions in calculations of the abundances of elements in very low-temperature plasmas. They will increase the recombination rate and hence its abundance, bringing it close to that obtained from collision strength.

These fine structure coupling effects in O II were not detected in the experiment [36, 37] because of its narrow energy range. However, such near threshold resonances have now been found in a recent ALS measurement of σ_{PI} of Se II, which has a similar electronic configuration as O II [38].

Similar is the case of excited $2s2p^3(\ {}^5S^o_2)$ state of Fe XXI [39], as shown in Fig. 7. Strong resonant structures below the core threshold ^4P state (pointed by arrow) are from relativistic fine structure couplings, not allowed in LS coupling. These resonances have been seen in measured recombination spectra.

5. Conclusion

There is a lack of large amount of highly accurate atomic data needed to resolve the existing discrepancies. Solar elemental abundances are widely discordant. Z-pinch experiments reveal problems in existing models. High-precision opacity is crucial to understand astrophysical conditions. Consideration of accurate radiative transitions and photo-ionization resonances, due to highly excited core states, have shown a larger absorption of radiation in accordance with the observed phenomena related to plasma opacities.

Acknowledgment

Partially supported by DOE-NNSA and NASA. Computations were carried out at the Ohio Supercomputer Center.

References

1. N.R. Simon. Astrophys. J. **260**, L87 (1982). doi:10.1086/183876.
2. M.J. Seaton. J. Phys. B, **20**, 6363 (1987). doi:10.1088/0022-3700/20/23/026.
3. The Opacity Project Team. The Opacity Project. Vol 1, 1995. Vol. 2. Institute of Physics Publishing. Bristol, UK. 1996.
4. F.J. Rogers and C.A. Iglesias. Astrophys. J. **340**, 361 (1992) . doi:10.1086/172066.
5. K.A. Berrington, P.G. Burke, K. Butler, M.J. Seaton, P.J. Storey, K.T. Taylor, and Y. Yan. J. Phys. B, **20**, 6379 (1987). doi:10.1088/0022-3700/20/23/027.
6. TOPbase. Available from http://cdsweb.u-strasbg.fr/topbase/topbase.html. Accessed 19 April 2011.
7. OPServer. Opacity project. Available from http://opacities.osc.edu.
8. D.G. Hummer, K.A. Berrington, W. Eissner, A.K. Pradhan, H.E. Saraph, and J.A. Tully. Astron. Astrophys. **279**, 298 (1993).
9. K.A. Berrington, W. Eissner, and P.H. Norrington. Comput. Phys. Commun. **92**, 290 (1995). doi:10.1016/0010-4655(95)00123-8.
10. TIPbase Opacity project. Available from http://cdsweb.u-strasbg.fr/topbase/topbase.html.
11. NORAD-Atomic-Data. Available from http://www.astronomy.ohio-state.edu/~nahar/nahar_radiativeatomicdata/index.html.
12. J.E. Bailey, G.A. Rochau, S.B. Hansen, P.W. Lake, T.J. Nash, D.S. Nielsen, R.D. Thomas, C.A. Iglesias, J. Abdallah, Jr., et al. 51st Annual meeting of the Division of Plasma Physics (DPP) of APS, Atlanta, Georgia, 2–6 November 2009. TOc.010.
13. S.N. Nahar and A.K. Pradhan. Astron. Astrophys. **437**, 345 (2005). doi:10.1051/0004-6361:20041885.
14. A.K. Pradhan and S.N. Nahar. Atomic astrophysics and spectroscopy. Cambridge University Press, Cambridge, UK. 2011. ISBN: 9780521825368.
15. W. Eissner, M. Jones, and H. Nussbaumer. Comput. Phys. Commun. **8**, 270 (1974). doi:10.1016/0010-4655(74)90019-8.
16. S.N. Nahar. Astron. Astrophys. **448**, 779 (2006). doi:10.1051/0004-6361:20053578.
17. S.N. Nahar, W. Eissner, G.X. Chen, and A.K. Pradhan. Astron. Astrophys. **408**, 789 (2003). doi:10.1051/0004-6361:20030945.
18. S.N. Nahar. Astron. Astrophys. **457**, 721 (2006). doi:10.1051/0004-6361:20065324.
19. S.N. Nahar. At. Data. Nucl. Data Tables. In press. 2011.
20. S.N. Nahar and A.K. Pradhan. Phys. Scr. **61**, 675 (2000). doi:10.1238/Physica.Regular.061a00675.
21. S.N. Nahar. Astron. Astrophys. Suppl. Ser. **147**, 253 (2000). doi:10.1051/aas:2000368.
22. National Institute for Standards and Technology (NIST). Available from http://www.nist.gov/pml/data/asd.cfm. Accessed 19 April 2011.
23. T. Shirai, J. Sugar, A. Musgrove, and W.L. Wiese. *In* Spectral data for highly ionized atoms: Ti, V, Cr, Mn, Fe, Co, Ni, Cu, Kr, and Mo. Journal of Physical and Chemical Reference Data, Monograph No. 8. 2000.
24. B.C. Fawcett. At. Data Nucl. Data Tables, **34**, 215 (1986). doi:10.1016/0092-640X(86)90003-3.
25. K.T. Cheng, Y.-K. Kim, and J.P. Desclaux. At. Data Nucl. Data Tables, **24**, 111 (1979). doi:10.1016/0092-640X(79)90006-8.
26. M. Loulergue, H.E. Mason, H. Nussbaumer, and P.J. Storey. Astron. Astrophys. **150**, 246 (1985).
27. V. Jonauskas, F.P. Keenan, M.E. Foord, R.F. Heeter, S.J. Rose, G.J. Ferland, R. Kisielius, P.A.M. van Hoof, and P.H. Norrington. Astron. Astrophys. **424**, 363 (2004). doi:10.1051/0004-6361:20040496.
28. J.P. Buchet, M.C. Buchet-Poulizac, A. Denis, A. Desesquelles, and M. Druetta. Phys. Rev. A, **22**, 2061 (1980). doi:10.1103/PhysRevA.22.2061.
29. Y. Сафронова. J. Quant. Spectrosc. Radiat. Transf. **15**, 223 (1975). doi:10.1016/0022-4073(75)90144-2.
30. U. Feldman, G.A. Doschek, R.D. Cowan, and L. Cohen. Astrophys. J. **196**, 613 (1975). doi:10.1086/153445.
31. M.W. Smith and W.L. Wiese. Astrophys. J. Suppl. Ser. **23**, 103 (1971). doi:10.1086/190235.
32. S.N. Nahar, G.X. Chen, and W. Eissner. Phys. Rev. A. (2011). In press.
33. Y. Yan and M.J. Seaton. J. Phys. B, **20**, 6409 (1987) . doi:10.1088/0022-3700/20/23/029.
34. S.N. Nahar, M. Montenegro, W. Eissner, and A.K. Pradhan. Phys. Rev. A**82**, 065401 (2010). doi:10.1103/PhysRevA.82.065401.
35. S.N. Nahar. Phys. Rev. A, **58**, 3766 (1998). doi:10.1103/PhysRevA.58.3766.
36. A.M. Covington, A. Aguilar, I.R. Covington, M. Gharaibeh, C.A. Shirley, R.A. Phaneuf, I. Alvarez, C. Cisneros, G. Hinojosa, et al. Phys. Rev. Lett. **87**, 243002 (2001). doi:10.1103/PhysRevLett.87.243002. PMID:11736500.
37. H. Kjeldsen, B. Kristensen, R.L. Brooks, F. Folkmann, H. Knudsen, and T. Andersen. Astrophys. J. Suppl. Ser. **138**, 219 (2002). doi:10.1086/323700.
38. N.C. Sterling, H.L. Dinerstein, S. Hwang, S. Redfield, A. Aguilar, M.C. Witthoeft, D. Esteves, A.L.D. Kilcoyne, M. Bautista, et al. Publ. Astron. Soc. Aust. **26**, 339 (2009) . doi:10.1071/AS08067.
39. S.N. Nahar. J. Quant. Spectrosc. Radiat. Transf. **109**, 2731 (2008). doi:10.1016/j.jqsrt.2008.07.007.